Infrared Physics and Technology 102 (2019) 103026

Contents lists available at ScienceDirect

Infrared Physics & Technology

journal homepage: www.elsevier.com/locate/infrared

Accuracy of activation energy from Arrhenius plots and temperature-dependent internal photoemission spectroscopy

Seyoum Wolde[a], Dilip Chauhan[a], Divya Somvanshi[a], A.G. Unil Perera[a,*], L.H. Li[b], Li Chen[b], S.P. Khanna[b], E.H. Linfield[b]

[a] Department of Physics and Astronomy, Georgia State University, Atlanta, GA 30303, USA
[b] The School of Electronic and Electrical Engineering, University of Leeds, Leeds LS2 9JT, UK

ARTICLE INFO

Keywords:
Activation energy
Arrhenius plot
Dark current
Internal photoemission
Temperature-dependent internal photoemission spectroscopy

ABSTRACT

In this work, the activation energy obtained from the temperature dependent internal photoemission spectroscopy (TDIPS) and thermionic dark currents using GaAs/AlGaAs photodetectors are compared. Different barrier heights within the *p*-type GaAs/AlGaAs heterostructures are studied. The temperature dependent spectral response shows the red-shifting of the detector threshold wavelength for increasing temperature due to the decreasing band-offset. The activation energy extracted from Arrhenius plot of the dark current-voltage-temperature (I-V-T), and measured spectral response show the carrier activation energy increases with increasing Al mole fraction and decreases with increasing doping density. For Infrared detectors with $\leq 6.5\,\mu m$, the Arrhenius analysis yields the values of activation energy with less than 5% deviation from the actual or TDIPS fitting values. However, for detectors with longer threshold wavelengths ($\gg 9.3\,\mu m$), activation energy extracted from the Arrhenius plot leads to energy values which deviate more than ~10% from the corresponding TDIPS values. The higher percentage deviation ($\gg 10\%$) of activation energy determined by Arrhenius plot from the corresponding TDIPS values attribute to the temperature dependent Fermi distribution tailing effect and Fowler–Nordheim tunneling current.

1. Introduction

The threshold wavelength, λ_t of an infrared (IR) photodetector, is one of the most important parameters from a detector operational point of view. This wavelength threshold of a photodetector is related to characteristic energy, $\Delta(eV) = 1.24/\lambda_t(\mu m)$, which is the minimum energy for a photoexcited carrier to overcome the barrier and contribute to the photocurrent. The design of different threshold wavelengths IR detector involves the selection of an appropriate potential barrier [1] and adjusting the Fermi level by changing the carrier concentration [2] or doping. A high doping density not only decreases the activation energy or increases the threshold wavelength but also increases the impurity scattering for the photoelectrons. High barrier or activation energy reduces the dark current and extends the dominant region of the thermionic emission current. This barrier height can be obtained from current-voltage-temperature (I-V-T), capacitance-voltage-temperature (C-V-T), and temperature-dependent internal-photoemission spectroscopy (TDIPS) [3] based on measured spectral responses. The comparison and difference between the apparent barrier heights obtained from C-V-T and I-V-T measurements are discussed in Song et al. [4,5] and others.

In this article, we compare two methods of determining the threshold wavelength or activation energy of *p*-type GaAs/$Al_xGa_{1-x}As$ to underline their respective advantages and disadvantages. The first method is based on the well-known Arrhenius analysis (or Richardson's plot) of the experimentally measured I-V-T characteristics of detectors. The thermionic emission (TE) model (Richardson-Dushman equation) for dark current at different temperature are used to investigate activation energy (threshold wavelength) at low electric field while Fowler-Nordheim (FN) or electric field emission (FE) models are briefly discussed at high electric fields. The activation energy extracted from Arrhenius plot provides information to predict the spectral response of detectors without carrying out spectral measurements. However, this standard thermionic emission theory predicts temperature independence of the barrier height [6] while this is not always the case experimentally. Hence, it is not always possible to determine the activation energy accurately for detectors displaying non-Arrhenius behaviors, such as strong temperature dependence of barrier height, tunneling and diffusion limited currents.

The neglected temperature dependence of activation energy (or

* Corresponding author.
E-mail address: uperera@phy-astr.gsu.edu (A.G.U. Perera).

https://doi.org/10.1016/j.infrared.2019.103026
Received 7 June 2019; Received in revised form 28 August 2019; Accepted 30 August 2019
Available online 30 August 2019
1350-4495/

Table 1
Parameters for samples under discussion. SP1, SP2, and SP3 vary only in Al mole fraction while SP1, LH1001, and LH1003 have nearly the parameters and vary in their doping levels.

Sample	Al Fraction	Barrier Thickness (nm)	Emitter Thickness (nm)	Doping N_A (cm^{-3})	Number of periods	Designed band offset(eV) at 78 K
SP1	0.28	60	18.8	3×10^{18}	30	0.157
SP2	0.37	60	18.8	3×10^{18}	30	0.207
SP3	0.57	60	18.8	3×10^{18}	30	0.319
LH1001	0.28	60	20	8×10^{18}	30	0.157
LH1003	0.28	60	20	6×10^{19}	30	0.157
LH1004	0.57	60	18.8	1×10^{19}	30	0.319

band offset) is revealed [3,7,8] in the past decade, by using internal photoemission (IPE) based methods [3,9]. The temperature-dependent internal-photoemission spectroscopy (TDIPS) [3] technique is one of the methods based on IPE process. IPE spectroscopy has been extensively used [3,10,11] to determine the interfacial barrier height (Δ) of different materials which defines the detector cutoff wavelength, λ_t as a function of detector parameters, temperature, and applied voltage. Now a days, TDIPS is a very useful [3] tool and used effectively to characterize the band offset parameters of different materials such as type-II InAs/GaSb superlattice (T2SL) [12,13] and MCT detectors [13–15], GaAs/AlGaAs heterojunctions [3,13,16,17], PtSi–Si diode [18], Si/HfO_2 interfaces [19], and a graphene-insulator-semiconductor structures [10,11].

The IPE process can be characterized by the quantum yield, defined as the number of emitted carriers per absorbed photons. Hence, the quantum yield in TDIPS is proportional to the product of measured spectral responsivity and photon energy [20]. Then, to obtain the activation energy or photoemission threshold (Δ), fittings to the yield spectra were carried out in the near-threshold regime at different temperatures. In the expression for quantum yield spectra, the transmission probability of carriers over the barrier, energy distribution function, and the temperature dependent band tailing effects are included. The carriers escape over the (AlGaAs in our case) barriers through an internal photoemission process and hence, TDIPS is sensitive to the temperature dependence of band offsets [3] (which is hardly possible in Arrhenius analysis). The advantage of TDIPS fittings is that only the spectral shape of the measured quantum yield determines the activation energy. Since the thermionic emission current is independent of the photon energy and only gives a constant background signal, the background can be distinguished from the yield spectra, by fitting the theoretical expression to the measured photoemission yield component alone.

The detailed inter-sub band transitions of holes in *p*-type GaAs/AlGaAs [20] and the temperature dependence of the band off set are revealed using the TDIPS fitting [3] technique. Therefore, the focus of this study is comparisons between activation energy determined by Arrhenius analysis and TDIPS fittings to underline the advantages/disadvantages of one over another in different temperature ranges for different barrier heights. The significant discrepancy in the values of the activation energy determined by Arrhenius technique and TDIPS fitting for a detector with longer threshold wavelength ($\gg 9.32\ \mu m$)is because Arrhenius analysis does not take the band tailing effect (sensitive to temperature variation) into account. In addition, Fowler–Nordheim (FN) tunneling current cannot be ignored for shallow barrier heights, like in the thermionic emission model used for Arrhenius analysis.

2. Device structures and experimental procedures

Set of *p*-type GaAs/$Al_xGa_{1-x}As$ heterostructure samples were grown with molecular beam epitaxy. The detectors demonstrated here are heterojunction interfacial work function internal photoemission (HEIWIP) detector which consists of alternative layers of highly *p*-doped absorbing GaAs (emitters) and undoped $Al_xGa_{1-x}As$ barriers. The active GaAs/$Al_xGa_{1-x}As$ regions are sandwiched between top and bottom (p^+-GaAs) ohmic contact layers. The highly *p*-doped and 18.8 nm thick GaAs emitters has three-dimensional energy states and heavy holes (hh),/light holes (lh) which are excited by incoming radiations as reported in Lao et al. [20]. These carriers escape over the AlGaAs barriers through an internal photoemission process occurring at the emitter-barrier interface. The internal work function is defined by the energy difference between the barrier bottom and the Fermi level (or the valence-band edge if the Fermi level is above it) of emitters and determines the threshold wavelength λ_t.

In GaAs/$Al_xGa_{1-x}As$ heterostructures, the doping density in the GaAs layers and the aluminum mole fraction (*x*), in the $Al_xGa_{1-x}As$ layers are some of the key factors that affect the mechanism or magnitudes of the dark current and photocurrent. Two important sets of experimental results based on doping and Al mole fraction have been compared (see Table 1). The first group is three heterostructures with the barriers having three x values giving rise to three different barrier heights. The Al mole fractions for the $Al_xGa_{1-x}As$ barrier in detectors SP1, SP2, and SP3 are 0.28, 0.37, and 0.57, respectively. In the second group, structures have three different doping levels. SP1, LH1001, and LH1003, have doping levels of $3 \times 10^{18}\,cm^{-3}$, $8 \times 10^{18}\,cm^{-3}$, and $6 \times 10^{19}\,cm^{-3}$, respectively while other parameters are the same. All the important parameters for various detector structures are summarized in Table 1.

The detectors were fabricated into square mesas of $400 \times 400\,\mu m^2$ with an optical window of $260 \times 260\,\mu m^2$ which allows front-side illumination. To characterize the detector, the square mesas and the ohmic contacts on the top and bottom layers were fabricated using standard wet chemical etching. Then the detector was mounted on the cold head of the liquid nitrogen-cooled Dewar or liquid helium-cooled cryostat to allow measurements of spectral response and dark current. Spectral measurements in the IR region for normal incidence radiation were carried out using a Perkin Elmer System 2000 Fourier transform infrared (FTIR) spectrometer while the dark current measurements were performed using the Keithley 2400 source meter. The temperatures were controlled and varied from 10 K to 300 K using Lake Shore 330 Auto tuning Temperature Controller with an accuracy of ± 0.01 K. A calibration of the sample temperature may be required if absorption of infrared light and position of temperature sensor causes appreciable temperature variations in the samples. However, such a variation is negligible in our experiment, as our temperature controller typically has the stabilization accuracy of $< \pm 0.1$ K.

3. Results and discussions

The temperature dependent spectral responses and I-V curves were measured at different temperatures. The temperature dependent spectral responses show a red-shift of detector threshold wavelength with increasing temperature. The effective interfacial barrier height (or activation energy) is extracted from the measured spectral response and I-V-T data using TDIPS fitting and Arrhenius analysis (plot) respectively. Arrhenius (or Richardson's plot) analysis gives valid results only for the temperature range where the thermionic emission is dominant and field emission (tunneling through the barrier) is negligible. Therefore, different analytical dark current models, such as thermionic emission (TE),

thermally assisted field emission (TFE) (or Fowler-Nordheim (FN) emission), and field enhanced thermal or Frenkel-Pool (FP) emission are briefly discussed for experimentally measured I-V-T data.

3.1. Thermionic emission

At low electric fields, for pure Ohmic behavior, the slope of ln(J) versus ln(V) approaches unity. At low field and high temperature, thermally excited carriers yield current with Ohmic characteristics that exponentially dependent on temperature. The current-voltage characteristics may be essentially assumed by the Richardson-Dushman model of thermionic emission, in which the carrier acquired a thermal energy sufficient to cross the barrier because of the superposition of the external and the image charge potential. This model is usually valid at lower fields and higher temperatures. Richardson-Dushman model that physically justifies the temperature dependence of dark current is

$$J = AT^{3/2}\exp(-\Delta/k_BT) \quad (1)$$

where the Δ is the activation energy and A is Richardson constant. At higher fields, the barrier height for thermionic emission is reduced, thus lowering the barrier height (or image force lowering). This effect is termed as Frenkel–Poole (FP) or Field-assisted thermal emission (FTE) as shown in Fig. 1. The activation energy in Eq. (1), with image force lowering considered, may be written as

$$\Delta = \Delta(0) - \sqrt{\frac{q^3F}{4\pi\,\epsilon_0\epsilon}} \quad (2)$$

where Δ(0), F, ε_o, ε are the interface potential barrier height or zero-field emission barrier height, the electric field, vacuum permittivity, and dielectric constant, respectively. As can be noted from the equation (1), the slopes of ln($J/T^{3/2}$) versus $1/k_BT$ at different voltages should be straight lines at high temperature ranges. Hence, for given electric field, the activation energy can be determined from experimentally measured J-V Arrhenius plot as

$$\Delta = \frac{d(J/T^{3/2})}{d(k_BT)} \quad (3)$$

This method is particularly valid for thermionic emission dominated

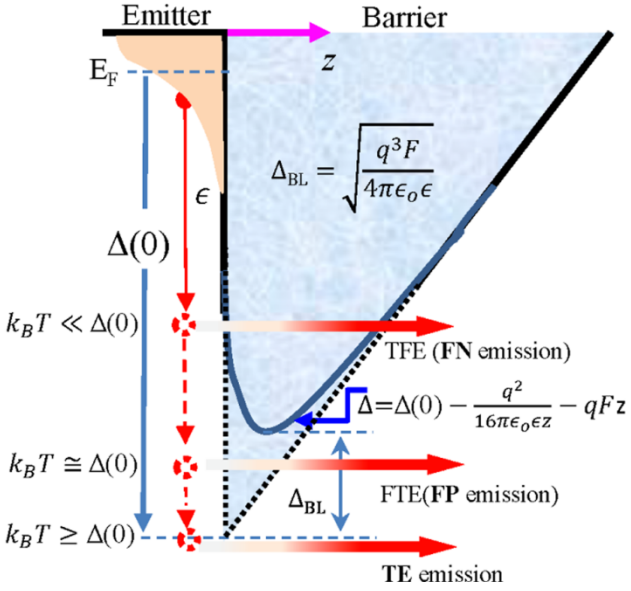

Fig. 1. The highly *p*-type doped GaAs (emitter) and AlGaAs (barrier) interfacial valence band profile under the influence of electric field. Assuming negligible pure tunneling current, the three transmission currents are due to thermally assisted (FN) emission, field enhanced (FP) thermal emission and thermal emission (TE).

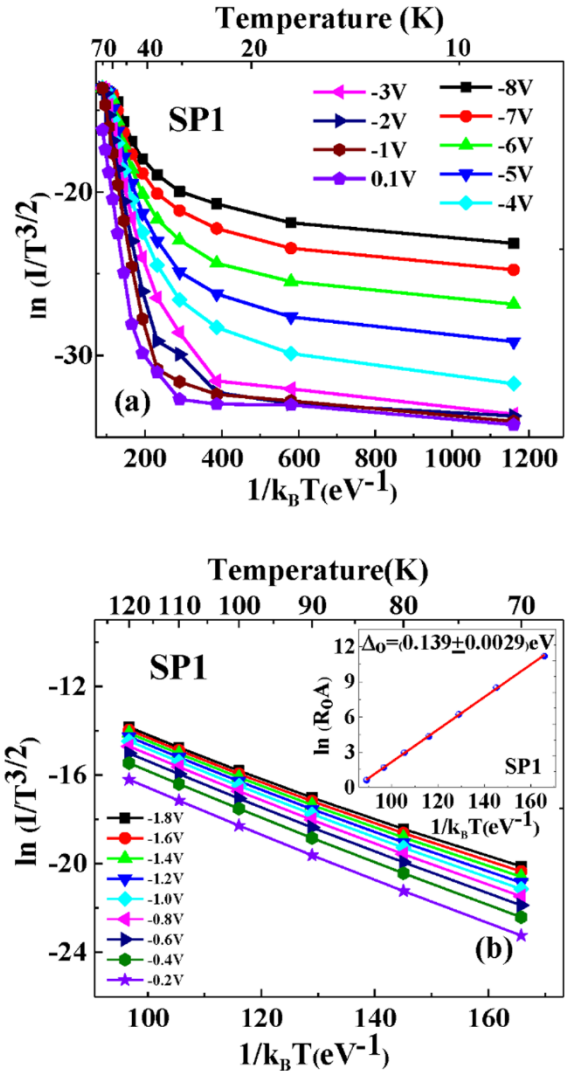

Fig. 2. Arrhenius plot for SP1 which has an Al fraction of 0.28 for (a) 40–130 K temperature ranges and (b) temperature range from 70 to 120 K. The inset in (b) is showing the Arrhenius plot for the relation $\ln(R_oA)\ \exp\left(-\frac{\Delta_0}{k_BT}\right)$.

behavior over a wide temperature range where the temperature dependence of the activation energy and tunneling current can be neglected. The two possible hypotheses that explain non-linearity of the ln ($J/T^{3/2}$) vs $1/k_BT$ plot are a strong temperature dependence of barrier height, which is not taken into account in the 3D drift current density model of thermal emissions and electric field assisted tunneling current, and/or the combination of the two effects.

Fig. 2(a) shows the ln ($J/T^{3/2}$) vs $1/k_BT$ characteristics for experimentally measured I-V-T for temperatures in the range10–130 K over a wide bias voltage range (0.1–8 V). For SP1 (x = 0.28) and for temperature, higher than ~70 K, excellent linear fits were obtained (see Fig. 2(b)) and this suggests that the exponential increase in the dark current with temperature is due to carrier thermal excitation to the higher energy states. In Fig. 2(a), for temperature lower than ~70 K, the dark current density is relatively insensitive to temperature, and is an attribute of phonon and electric field assisted tunneling. The activation energy at (or near) zero electric field can also be calculated from the dark current-voltage characteristics using the Arrhenius plot for the relation $R_oA\ \exp\ (\Delta_0/k_BT)$ where Δ_o is the activation energy at zero field, $R_o = \left(\frac{dJ}{dV}\right)^{-1}_{V=0}$ and A is the area of the detector.

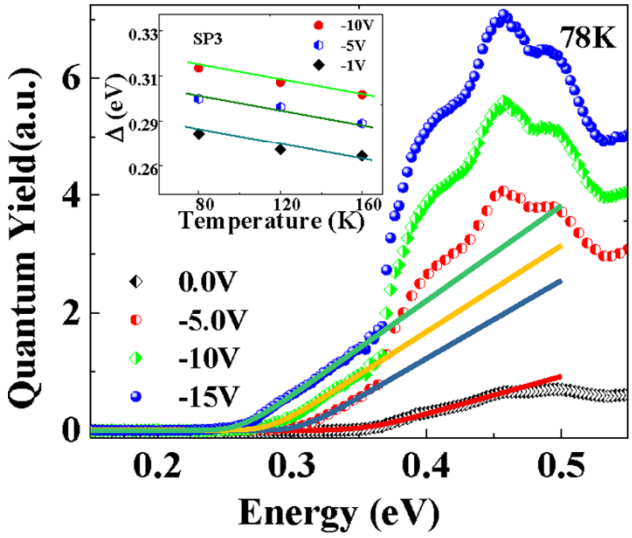

Fig. 3. Solid lines are TDIPS fitting for experimental quantum yield spectra of SP3 at 78 K for four different biases. Inset shows the temperature dependence of activation energy based on TDIPS fittings to the experimentally measured response spectra.

3.2. Temperature-dependent internal-photoemission spectroscopy (TDIPS)

The valence band offsets (ΔE_v) of *p*-type GaAs/$Al_xGa_{1-x}As$ heterostructures (Table 1) and their temperature dependence were obtained through analyzing quantum yield spectra measured at different temperatures. The quantum yield is proportional to the product of photon energy and measured spectral response [3,20]. The spectral shape of the quantum yield near the threshold regime plays a crucial role to determine the activation energy. Therefore, the dominant processes affecting the energy distribution of carriers and their escape probabilities across the interface will lead to the required expression for the quantum yield. The quantum yield Y($h\nu$) in terms of the photoexcitation of holes in the emitter through inter-valence-band (IVB) transitions [20], described by an energy distribution function $\rho(\epsilon, h\nu - E_F)$, and the transmission of holes over the barrier, described by a probability function of $P(\epsilon, \Delta)$ reads as [3],

$$Y(h\upsilon) = Y_0(KT) + C_0 \int_{\Delta}^{\infty} \rho(\epsilon, h\nu - E_F) f(\epsilon, h\nu) P(\epsilon, \Delta) d\epsilon \quad (4)$$

where C_0 is a constant independent of ϵ and $h\nu$. ϵ is the energy of photoexcited holes. Δ is the required activation energy. The energy is scaled downward with the zero reference at the Fermi level. Eq. (4) describes the case of degenerate (highly) doped emitters (E_f lying within the VB). At finite temperatures; carriers occupy energy states above the Fermi level in terms of the Fermi-Dirac (FD) statistics. An FD function $f(\epsilon, h\nu) = [1 + \exp(\epsilon - h\nu)/KT]^{-1}$ was used as the

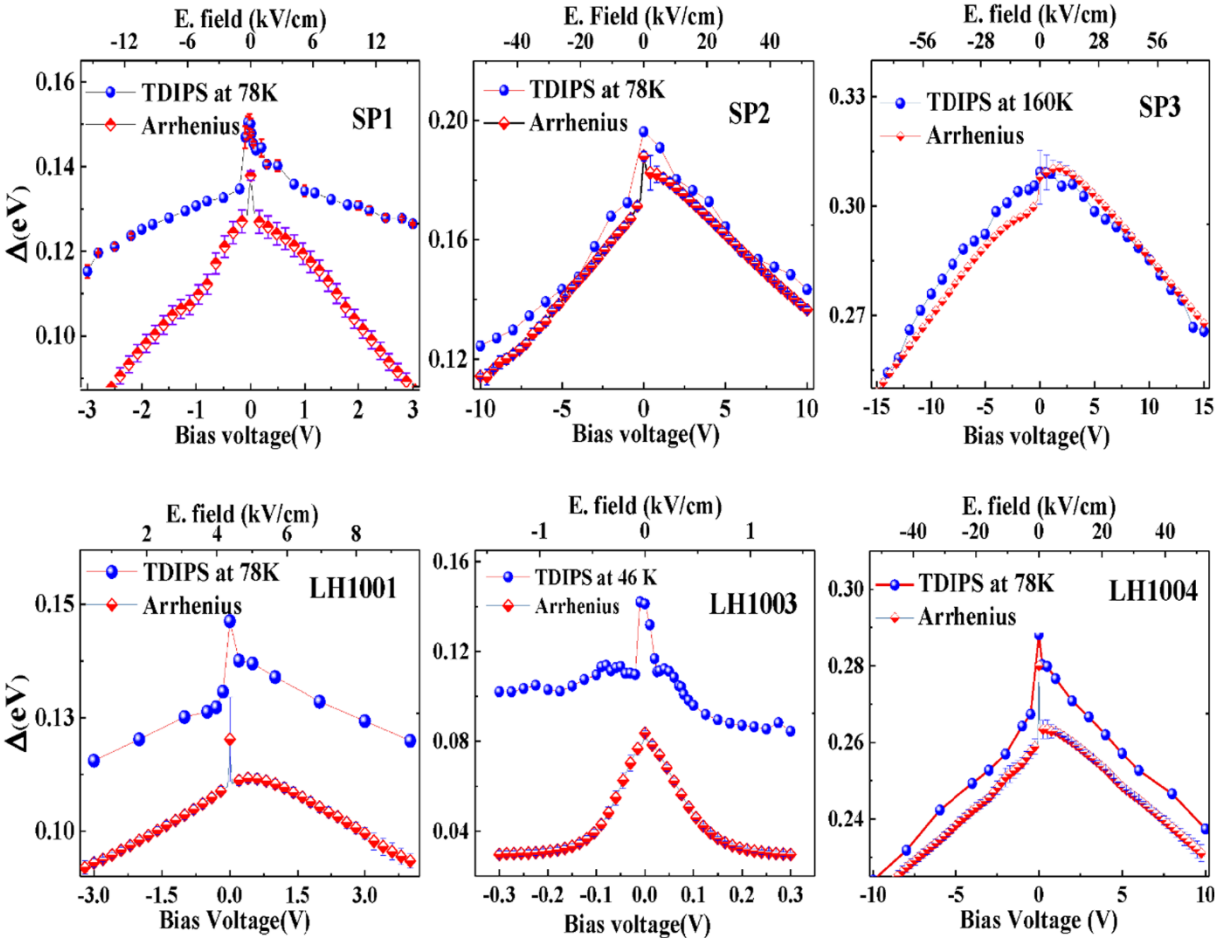

Fig. 4. Comparisons between activation energies determined by TDIPS fitting and Arrhenius plot for samples with different Al fraction and doping levels. SP1, SP2, SP3 have different Al fraction and SP1 with least Al fraction (or least barrier height) displays significant disparity. SP1, LH1001, and LH1003 have different doping levels while nearly same other parameters. For devices of threshold wavelength longer than ~9.3 μm, the activation energy determined by Arrhenius plot is way off from TDIPS fitting results. The activation energy determined by Arrhenius plot for devices with shorter threshold wavelength (≪9.3 μm), SP2, SP3, and LH1004, agree well with the measured threshold spectral response.

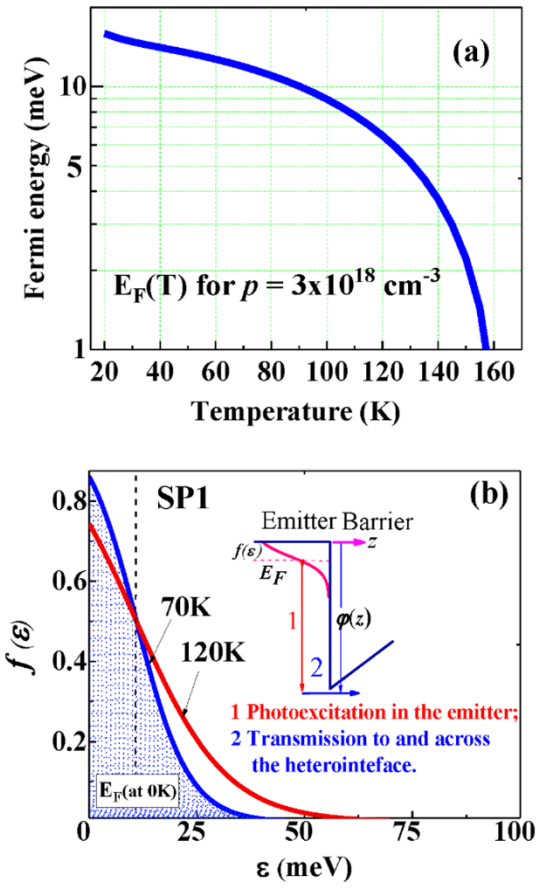

Fig. 5. Temperature dependence of (a) Fermi level (b) Fermi distribution functions versus carriers' energy, ε. The FD tail increases with temperature and extends up to ~100 meV for T = 120 K. The inset shows photoexcitation in the *p*-emitter and transition to and across the i-barrier or hetero-interface in the IPE processes.

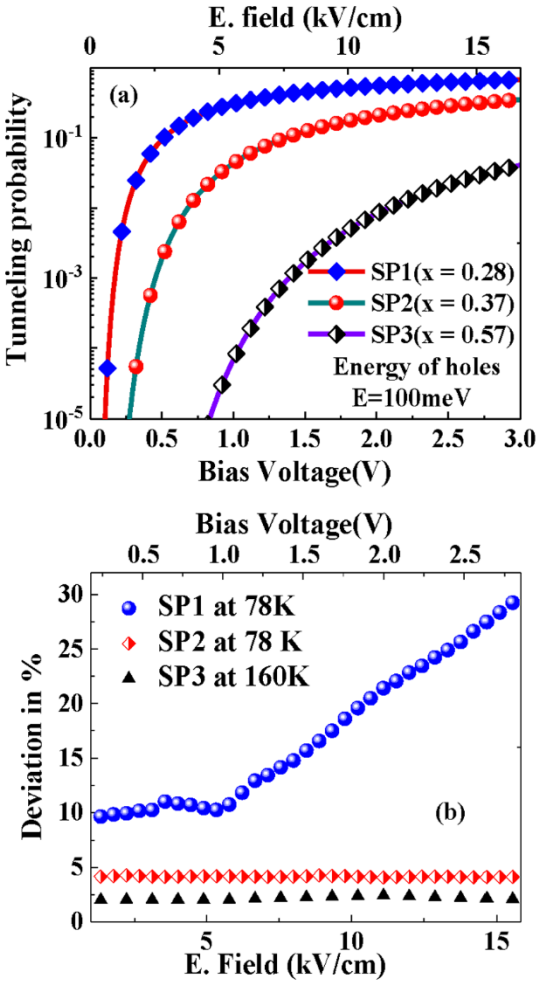

Fig. 6. (a) The tunneling probability of holes with 100 meV energy as a function of bias voltage for three different barrier heights. (b) The deviation of activation energy determined by Arrhenius from TDIPS.

distribution function. This assumes that the photoexcited holes remain in the same distribution as before the photoexcitation, with the only difference in energy by $h\nu$. To obtain the photoemission threshold (Δ), fittings to the yield spectra (~product of photon energy and response) were carried out in the near-threshold regime by using Eq. (4) and the Levenberg-Marquardt fitting algorithm, where Y_0, C_0, and Δ are regarded as fitting parameters. E_f was determined by carrying out an $8 \times 8\,\boldsymbol{k}\cdot\boldsymbol{p}$ computation [21] and integrating the product of density of state by the FD distribution function over the entire range of energies.

Based on TDIPS fitting results, the valence band off-set of GaAs/$Al_xGa_{1-x}As$ heterostructures (in eV) is given by [3] $\Delta E_V = (0.57 - 1.39x10^{-4} \times T)x$, where T is in Kelvin. Based on this equation, the designed band off set of samples at 78 K is shown in the last column of Table 1. The activation energy or photoemission threshold at 0 V is then given by $\Delta(0\text{ V}) = \Delta E_v - \Delta_{BGL} - E_f$, where Δ_{BGL} is the band gap lowering due to electric field is shown in Fig. 1. In Fig. 3, the solid lines show TDIPS fittings to spectral responses of SP3 at 78 K for different bias voltages and inset shows the temperature dependence of activation energy based on TDIPS fittings to experimentally measured spectral response. The activation energy decreases (red shift) with increasing bias in an exponential form, due likely to energy band bending [22,23] and with increasing temperature due to decreasing band offset. Fig. 4 shows the activation energies extracted from Arrhenius plot and TDIPS fitting for samples described in Table 1.

3.3. Temperature dependent Fermi distribution and tail effect

For highly doped HEIWIP, the temperature dependence of Fermi level E_F is given by [6]

$$E_v - E_F = k_B T\left[ln\left(\frac{p}{N_v}\right) + 2^{-\frac{3}{2}}\left(\frac{p}{N_v}\right)\right] \quad (5)$$

where p is the doping density (cm^{-3}) level, the temperature dependent density of states (cm^{-3}) for GaAs in the valence band $N_v = 2\left(\frac{m^* k_B T}{2\pi\hbar^2}\right)^{\frac{3}{2}}$ and the density-of-state effective mass of valence band[6], $m^* = (m_{lh}^{3/2} + m_{hh}^{3/2})^{2/3}$. Hence, $N_v = 1.87233 \times 10^{15}\ T^{3/2}$. At zero electric field, the temperature dependence of activation energy or effective barrier height $\Delta(T)$ is given by $\Delta(T) = \Delta E_v(T = 0K) - E_F(T)$, where $\Delta E_v(T = 0K)$ is the barrier height at 0 K. For temperature change from 60 K to 120 K, the change in fermi level is $\Delta E_F(T) \cong 0.0062\ eV$, which is 4.1%, 3.3%, and 2.0% of the barrier height calculated at intermediate temperature (80 K) for SP1, SP2, and SP3 respectively. This implies that the temperature dependence of fermi level shown in Fig. 5(a), has little effect on these barrier heights. However, Fig. 4 shows, there are significant differences between the activation energy obtained from Arrhenius plot and TDIPS fittings for structures with least (0.28) Al mole fraction (SP1, LH1001, and LH1003) and highest doping level (LH1003; 6×10^{19} cm^{-3}). This disparity of the two results may be due to the non-linear temperature dependence of Δ over a wide range of temperatures and hence is the effect of the temperature dependent band tailing effect shown in Fig. 5(b) and Fowler-Nordheim tunneling.

The Fermi-Dirac occupation probability $f(\epsilon)$ of carriers with energyϵ, is given by

Table 2
The percentage deviation of Arrhenius Δ from the corresponding TDIPS Δ near zero bias and at bias voltage of 1 V (5.4 kV/cm) except 0.1 V (0.54 kV/cm) for LH1003. As the threshold wavelength increases from 4 μm to 12.9 μm, the deviation of activation energy determined by Arrhenius plot from TDIPS fitting values increases.

Sample	Minimum Average Temp (K) for Arrhenius	Temp. (K) for TDIPS Δ	λ_t (μm) at 1.0 V (5.4 kV/cm)	Near zero bias voltage			At 1.0 V (5.4 kV/cm) except 0.54 kV/cm for LH1003.		
				Arrhenius Δ(eV), $\partial(\ln(R_oA))/\partial\left(\frac{1}{k_BT}\right)$	TDIPS Δ(eV)	|Arrh-TDIPS|Δ	ArrheniusΔ(eV), $\partial(\ln(J/T^{1.5}))/\partial\left(\frac{1}{k_BT}\right)$	TDIPS Δ(eV)	Arrh-TDIPS|Δ
SP3	140	160	4.03 ± 0.01	0.303 ± 0.002	0.309	1.9%	0.309 ± 0.003	0.307 ± 0.001	0.3%
LH1004	120	78	4.48 ± 0.02	0.280 ± 0.003	0.288	2.8%	0.266 ± 0.002	0.277 ± 0.001	4.0%
SP2	120	78	6.53 ± 0.03	0.188 ± 0.002	0.196	4.0%	0.182 ± 0.002	0.190 ± 0.001	4.2%
SP1	70	78	9.32 ± 0.21	0.139 ± 0.003	0.150	7.3%	0.120 ± 0.002	0.133 ± 0.003	9.7%
LH1001	60	78	9.61 ± 0.22	0.120 ± 0.006	0.146	17.8%	0.110 ± 0.003	0.129 ± 0.003	15.4%
LH1003	40	46	12.92 ± 0.4	0.084 ± 0.005	0.141	40.4%	0.048 ± 0.003	0.096 ± 0.003	50.6%

Table 3
Summary of results: The deviation of activation energy extracted from TDIPS fitting and Arrhenius plot for different wavelength ranges. The accuracy of Arrhenius plot is expressed in terms of deviation from the corresponding TDIPS fitting. The accuracy of TDIPS fitting depends on the accuracy of spectral response measurement.

λ_t (μm)	TDIPS	Arrhenius
3 – ~5 (MIR)	Valid at any operating temperature	Deviate up to maximum of ~5% at temp. higher than ~120 K.
5 – ~9.3	Valid at any operating temperature	Deviate up to maximum of ~10% at temp higher than ~70 K and e. field F ≪5.4 kV/cm.
> 9.3	Valid at any operating temperature	Not valid irrespective of temperature and electric field.

$$f(\epsilon) = [1 + \exp(\epsilon - E_F/k_BT)]^{-1} \quad (6)$$

The Fermi-Dirac distribution (FD) shows very small tail above the Fermi level at 0 K even at low temperatures (5–10 K). As the temperature increases, the occupation probability of carriers above the Fermi level at 0 K increases and the tail extend near to the edge of small barrier heights such as SP1 (with Al mole fraction of 0.28) and LH1003 (0.28 Al mole fraction and highest doping levels (6×10^{19} cm^{-3})) as shown in Fig. 5(b). Hence, this tail has some profound effects on thermionic emission for temperature such as 70 K and 120 K for smaller band offset ($\lesssim 0.157\ eV$) such as SP1, LH1001, and LH1003. As has been shown in Fig. 5(b), this significant change in tail for temperature as low as 40 and 70 K, determine and affect the activation energy of photoexcitation in the emitter.

3.4. Field emission

Field emission is a quantum mechanical tunneling process. The non-Arrhenius behavior of longer threshold wavelength detectors can also be explained by thermally assisted field emission or Fowler-Nordhiem (FN) tunneling current. The current density (J_{Tun}) induced by holes tunneling in the z- or growth direction through a barrier shown in Fig. 1 is given by Eq. (7).

$$J_{Tun} = \frac{qm^*k_BT}{2\pi^2\hbar^3}\int_0^\infty T(\epsilon_z, F)ln(1 + e^{(\epsilon_z - E_f)/k_BT})d\,\epsilon_z \quad (7)$$

where the Wentzel-Kramers-Brillouin (WKB) Method is a way of determining the transmission probability T(ϵ_z, F) of holes through a "slowly" varying potential [6,24,25] as

$$T \cong exp\left(-2\int_{z_0}^{z_1}\sqrt{\frac{2m^*}{\hbar^2}(\varphi(z) - \epsilon_z)}dz\right) = exp(-B(\epsilon_z)) \quad (8)$$

Since this approach yields value of T = 1 for energies above the maximum value of qV, where V is the voltage, it doesn't include quantum mechanical reflection in these cases. This means that it overestimates the current for shallow barriers and cannot handle the case of a zero barrier at the interface. An alternate method of derivation of the transmission probability yields an expression with identical exponent but slightly different form of Eq. (8) [26]. This alternate expression is far more accurate near and above the top of the barrier [27].

$$T(\epsilon, F)_{WKBtype} \cong \frac{1}{1 + exp(-B(\epsilon))} \quad (9)$$

In general, this expression isn't often used because when multiplied by another function it is often un-integrable.

However, with a series of reasonable approximations, it becomes very useful. The tunneling probability shown in Fig. 6(a) and (b) with increasing deviation at the field around 5 kV/cm confirms that the FN tunneling current cannot be ignored for lower barrier height of SP1 (x = 0.28). Similarly, Yang et al. demonstrated that tunneling currents in InAs/(GaIn)Sb superlattice photodiodes are important issues for photodetectors operating in the long-wavelength (> 8 μm) range [28–30].

The temperature range for the thermionic current to be dominant (or only thermionic) varies with bias voltage (electric field) and barrier heights. One can roughly estimate the minimum average temperature for which thermionic current starts to be dominant. Fig. 2(b) shows the linear part of plots in Fig. 2(a) where the dark current is dominant or only due to thermionic emission. Then the Arrhenius plot can be used to extract the activation energy for the temperature range starting from this minimum average temperature (column two of Table 2) to the highest temperature within maximum current limit (~1 mA) of the measurements. Based on the experimental results shown in Fig. 4 and Table 2, the percentage deviation of activation energy of Arrhenius plot from the corresponding TDIPS fitting values at (or near) zero bias and at bias voltage of 1 V (5.4 kV/cm) except 0.1 V (0.54 kV/cm) for LH1003 is related to the threshold wavelength of the detectors. For SP1, SP2, and SP3, the activation energy increases with increasing Al mole fraction (0.28, 0.37, and 0.57 respectively). However, for SP1, LH1001 and LH1003, the activation energy decreases with increasing doping levels (3×10^{18} cm^{-3}, 6×10^{18} cm^{-3}, 6×10^{19} cm^{-3} respectively).

As the threshold wavelength increases from 4 μm to 12.9 μm, the deviation of activation energy determined by Arrhenius plot from the corresponding TDIPS fitting values increase; for example, from 0.3% (at 160 K) to 50.6% (at 46 K).

A summary of these results is shown in Table 3. For detectors with ~6.5 μm or shorter threshold wavelength, the Arrhenius analysis yields the values of activation energy within 5% deviation from that of TDIPS. Even though Arrhenius plot is valid in general at low field (near zero volts) over a certain temperature range, a significant deviation from TDIPS fitting values are observed due to the Fermi distribution tail (see

Fig. 5(b)) that extends up to the edge of the lowest band offset (0.157 eV) detectors (SP1, LH1001 and LH1003) for the minimum average temperatures of thermionic current shown in the second column of Table 2. The Arrhenius plot used to extract activation energy of detectors with threshold wavelength longer than ~9.3 μm, where the FN tunneling, and Fermi tailing effects cannot be ignored, such as in SP1, LH1001, and LH1003, does not lead to precise values, nor does it represent any parameters of carriers' energy.

4. Conclusion

Different barrier heights within the GaAs/AlGaAs heterostructures are evaluated. As the threshold wavelength of detector increases from 4 μm to 12.9 μm, the deviation of activation energy determined by Arrhenius plot from the corresponding TDIPS fitting value increases. For detectors with ~6.5 μm or shorter threshold wavelength, the Arrhenius analysis yields the values of activation energy with less than 5% deviation. However, for detectors with longer threshold wavelength (≫9.3 μm), the Arrhenius plot used to extract activation energy leads to energy values with deviation higher than ~10%. The higher percentage deviation (> 10%) of activation energy determined by Arrhenius plot from the corresponding TDIPS values attribute to the temperature dependent Fermi distribution tailing effect and Fowler–Nordheim tunneling current. Therefore, if a precise band off-set characterization of long threshold wavelength detector is needed, it is inevitable to use a more accurate method than the Arrhenius. In that case, TDIPS that takes the temperature dependence of activation energy in to account will satisfy the requirements over a wide range of threshold wavelength. However, still Arrhenius is simple and a reasonable tool to characterize detector with shorter threshold wavelength(≪9.3 μm).

Acknowledgments

This work was supported by the U.S. Army Research Office [Grant No. W911 NF-15-1-0018]. Funding was also received from the European Community's Seventh Framework Programme (FP7-IDEAS-ERC) [Grant agreement No. 247375 'TOSCA']. Seyoum Wolde and Edmund Linfield acknowledge support from the GSU Center for Diagnostics and Therapeutics Fellowship, and the Royal Society and Wolfson Foundation, respectively and appreciate T. Park for the technical support.

Appendix A. Supplementary material

Supplementary data to this article can be found online at https://doi.org/10.1016/j.infrared.2019.103026.

References

[1] H. Schneider, Quantum Well Infrared Photodetectors, Springer, Berlin, 2007.
[2] A.G.U. Perera, W. Shen, GaAs homojunction interfacial workfunction internal photoemission (HIWIP) far-infrared detectors, Opto-Electron. Rev. 7 (1999) 153.
[3] Y.-F. Lao, A.U. Perera, Temperature-dependent internal photoemission probe for band parameters, Phys. Rev. B 86 (2012) 195315.
[4] Y. Song, R. Van Meirhaeghe, W. Laflere, F. Cardon, On the difference in apparent barrier height as obtained from capacitance-voltage and current-voltage-temperature measurements on Al/p-InP Schottky barriers, Solid-State Electron. 29 (1986) 633–638.
[5] R. Kumar, S. Chand, Fabrication and electrical characterization of nickel/p-Si Schottky diode at low temperature, Solid State Sci. 58 (2016) 115–121.
[6] S.M. Sze, K.K. Ng, Physics of Semiconductor Devices, Wiley, 2006.
[7] K. Malloy, J. Van Vechten, Temperature dependence of the mercury telluride-cadmium telluride band offset, Appl. Phys. Lett. 54 (1989) 937–939.
[8] C. Becker, V. Latussek, A. Pfeuffer-Jeschke, G. Landwehr, L. Molenkamp, Band structure and its temperature dependence for type-III H g T e/H g 1–x Cd x Te superlattices and their semimetal constituent, Physical Review B 62 (2000) 10353.
[9] J. Helman, F. Sanchez-Sinencio, Theory of internal photoemission, Phys. Rev. B 7 (1973) 3702.
[10] R. Yan, Q. Zhang, W. Li, I. Calizo, T. Shen, C.A. Richter, et al., Determination of graphene work function and graphene-insulator-semiconductor band alignment by internal photoemission spectroscopy, Appl. Phys. Lett. 101 (2012) 022105.
[11] Y. Hikita, M. Kawamura, C. Bell, H. Hwang, Electric field penetration in Au/Nb: SrTiO 3 Schottky junctions probed by bias-dependent internal photoemission, Appl. Phys. Lett. 98 (2011) 192103.
[12] Y.-F. Lao, P. Pitigala, A. Unil Perera, E. Plis, S. Krishna, P.S. Wijewarnasuriya, Band offsets and carrier dynamics of type-II InAs/GaSb superlattice photodetectors studied by internal photoemission spectroscopy, Appl. Phys. Lett. 103 (2013) 181110.
[13] Y.-F. Lao, A.U. Perera, Physics of internal photoemission and its infrared applications in the low-energy limit, Adv. OptoElectron. 2016 (2016).
[14] Y.-F. Lao, A. Unil Perera, P.S. Wijewarnasuriya, Optical study of HgCdTe infrared photodetectors using internal photoemission spectroscopy, Appl. Phys. Lett. 104 (2014) 131106.
[15] A. Perera, Y. Lao, P. Wijewarnasuriya, S. Krishna, Band Offsets of III–V and II–VI Materials Studied by Temperature-Dependent Internal Photoemission Spectroscopy, J. Electron. Mater. 45 (2016) 4626–4630.
[16] Y.-F. Lao, A. Unil Perera, Y. Zhang, T. Wang, Band-offset non-commutativity of GaAs/AlGaAs interfaces probed by internal photoemission spectroscopy, Appl. Phys. Lett. 105 (2014) 171603.
[17] A. Perera, Heterojunction and superlattice detectors for infrared to ultraviolet, Prog. Quantum Electron. 48 (2016) 1–56.
[18] B. Aslan, R. Turan, On the internal photoemission spectrum of PtSi/p-Si infrared detectors, Infrared Phys. Technol. 43 (2002) 85–90.
[19] V. Afanas' ev, A. Stesmans, F. Chen, X. Shi, S. Campbell, Internal photoemission of electrons and holes from (100) Si into HfO 2, Appl. Phys. Lett. 81 (2002) 1053–1055.
[20] Y. Lao, P. Pitigala, A. Perera, H. Liu, M. Buchanan, Z. Wasilewski, et al., Light-hole and heavy-hole transitions for high-temperature long-wavelength infrared detection, Appl. Phys. Lett. 97 (2010) 091104.
[21] T.B. Bahder, Eight-band k.p model of strained zinc-blende crystals, Phys. Rev. B 41 (1990) 11992.
[22] A.G.U. Perera, S.G. Matsik, B. Yaldiz, H.C. Liu, A. Shen, M. Gao, et al., Heterojunction wavelength-tailorable far-infrared photodetectors with response out to 70 μm, Appl. Phys. Lett. 78 (2001) 2241.
[23] D.H. Zhang, W. Shi, Dark current and infrared absorption of p-doped InGaAs/AlGaAs strained quantum wells, Appl. Phys. Lett. 73 (1998) 1095.
[24] D.A.B. Miller, Quantum Mechanics For Scientists And Engineers, 7th ed., Cambridge University Press, New York, 2014.
[25] E.L. Wolf, Tunneling spectroscopies of metal and semiconductor phonons, in: P.K. Hansma (Ed.), Tunneling Spectroscopy: Capabilities, Applications, and New Techniques, Springer, US, Boston, MA, 1982, p. 71.
[26] S.C. Miller Jr., R. Good Jr., A WKB-type approximation to the Schrödinger equation, Phys. Rev. 91 (1953) 174.
[27] R.G. Forbes, J.H.B. Deane, Reformulation of the standard theory of Fowler–Nordheim tunnelling and cold field electron emission, Proceedings of the Royal Society A: Mathematical, Physical and Engineering Science, 2007, p. 2907.
[28] Q. Yang, F. Fuchs, J. Schmitz, W. Pletschen, Investigation of trap-assisted tunneling current in InAs/(GaIn) Sb superlattice long-wavelength photodiodes, Appl. Phys. Lett. 81 (2002) 4757–4759.
[29] L. Bürkle, F. Fuchs, E. Ahlswede, W. Pletschen, J. Schmitz, Wannier-Stark localization in InAs/(GaIn) Sb superlattice diodes, Phys. Rev. B 64 (2001) 045315.
[30] M. Reine, A. Sood, T. Tredwell, Photovoltaic infrared detectors, Semiconductors and Semimetals, Elsevier, 1981, pp. 201–311.